Research Article

Achieving maximum strength-ductility combination in fine-grained Cu-Zn alloy via detwinning and twinning deformation mechanisms

Lei Gu, Ningning Liang*, Yuyao Chen, Yonghao Zhao*

Nano and Heterogeneous Materials Center, School of Materials Science and Engineering, Nanjing University of Science and Technology, Jiangsu 210094, China

ARTICLE INFO

ABSTRACT

Although deformation twinning has been demonstrated to improve the strain hardening and ductility of metals and alloys with low stacking fault energies (SFEs), the optimum grain size for maximum strength-ductility combination still needs to explore. In this work, we selected Cu- 30 wt% Zn alloy with extremely low SFE (7 mJm^{-2}) acting as a model material. Specifically, Cu- 30 wt% Zn samples with different grain sizes ranging from 628 nm to 30.6 μm were prepared by equal-channel-angular pressing (ECAP) and subsequent annealing. Tensile test revealed that the maximum strength-ductility combination (ultimate tensile strength of 565 MPa and ductility of 20%) corresponds to a mean grain size of 3.8 μm. Electron backscatter diffraction (EBSD) indicated that pre-existing annealing twins in fine-grained Cu- 30 wt% Zn alloy annihilated at the initial deformation stage (<10% tensile strain) via detwinning of thin twin lamellae (<1 μm) and conversion of twin boundaries of thick twin lamellae (>1 μm) into conventional high-angle grain boundaries. In the later stage of deformation (>10% strain), deformation twinning occurred in grains with <111> orientation parallel to tensile direction, suggesting the combination of both detwinning and twinning deformations caused the maximum strength and ductility synergy. Our findings provide insights into optimization of strength and ductility of metals with low SFEs and detwinning-twinning deformation mechanisms.

© 2022 Elsevier B.V. All rights reserved.

1. Introduction

Face-centered cubic (fcc) metals and alloys with low stacking fault energies (SFEs), such as Fe-Mn based alloys [1–5], Cu alloys [6–10], high- and medium-entropy alloys [10–18], have been widely reported to possess high tensile strength, good ductility and enhanced strain hardening rate due to twinning-induced-plasticity (TWIP) and transformation-induced-plasticity (TRIP) effects. For example, the SFE of pure Cu (~78 mJm^{-2}) can be significantly reduced by alloying with the addition of Al contents (Cu- 0.86 wt% Al: ~38 mJm^{-2}; Cu- 2.2 wt% Al: ~20 mJm^{-2}) and the lower SFEs provided more TWIP effect [6–10]. For high-entropy Cantor alloy, by manipulating the atomic composition ratio, the SFEs can be further reduced less than 10 mJm^{-2} and the tensile properties were therefore improved [16–18]. Compared to metals with high SFEs, such as pure Al [19,20], Cu [21], Ni [22,23], etc., alloys with low SFEs have the significantly improved strain hardening capacity due to TWIP and TRIP effects.

Inspection of literatures indicated that traditional strengthening mechanisms by introducing grain boundaries (GBs) and dislocation substructures unexceptionally result in dramatically decreased ductility [24–26]. On contrast, introducing high-density twin boundaries (TBs) in materials increases the yield strength (YS) without sacrificing ductility too much [27,28]. Lu et al. [27] reported that the nano-twinned Cu possesses a high YS of 980 MPa and a basically equivalent ductility (13%) compared with ultrafine-grained (UFG) Cu counterpart due to the pre-existing nanoscale twin lamellae in sub-micrometer-sized grains. Similarly, Duan et al. [29] fabricated nano-twinned Ni with an ultra-high strength of 4 GPa and an average twin thickness of 2.9 nm. The authors attributed the strengthening to the much more stable TBs than conventional GBs because TBs are effective barrier on the nucleation and motion of dislocations [30]. Not only pre-existing twins can improve the strength [27,28], deformation twinning can also significantly enhance the ultimate tensile strength (UTS) and ductility by blocking and accumulating dislocations during plastic deformation process [6–10]. More recently, Liu et al. [31] found that numerous deformation twins formed in Cu-Zn alloys with low SFE during surface mechanical attrition treatment. These twins further formed the

accumulation of geometrically necessary dislocations (GNDs) and strong hetero-deformation induced (HDI) hardening effect.

According to the traditional dislocation theory, a full dislocation in fcc crystals tends to dissociate into two partial dislocations on the {111} plane in order to lower its energy. With the reduction of the SFEs, the separation distance between the partial dislocations becomes larger, contributing to increased twinning tendencies. Szczerba et al. [32] found that deformation twinning was activated at the range of the SFEs between 4 mJm^{-2} (the lower SFE limit) and 7.5 mJm^{-2} (the upper SFE limit) in Cu-Al single crystals under tension. When the SFE is lower than 4 mJm^{-2}, the crystal lattice shear was produced by slip prior to twinning due to the incremental twinning stress. Our previous investigations systermetically revealed that twin nucleation size (i.e. twin thickness) of Cu-Al and Cu-Zn alloys increases first and then decreases with decreasing SFEs, that is, there exists an optimum SFE for twin nucleation [33]. In addition to SFE, microstructures such as grain size and grain orientation may also influence the twinning stress. Systematic studies about the grain size effect on deformation twinning have been reported in Refs. [34,35]. In the coarse-grained region, deformation twinning becomes more difficult with decreasing grain size due to the rapidly increased critical stress for twinning. However, in the nanocrystalline (nc) region, there exists an optimum grain size range for the activation of deformation twinning [34,35]. Moreover, twin thickness was found to decrease with decreasing grain size, and when the grain size is smaller than about 20 nm for Cu- 30 wt% Zn alloy, stacking faults with one atomic layer can only form [36,37]. Our more recent studies also revealed ternary relation among SFE, grain size and twin nucleation size in nc and UFG Cu-Al and Cu-Zn alloys [33,38–40]. In addition to the grain size, it is well known that many external factors, for instance, deformation temperature and strain rate, may influence the deformation twinning [41,42].

Deformation-induced detwinning deformation in fcc metals and alloys has been observed under tension-compression cyclic loading experiments [43–46]. In a Cu-Al single crystal, a layered twin-matrix sample was obtained by specially designed uniaxial tension, and during uniaxial compression detwinning occurred [43]. Szczerba et al. found that the detwinning was activated in a confined area where a localized deformation region was created in the form of kink bands and the crystal lattice rotation was also generated [44]. Recently, in-situ direct observation of twinning/detwinning in a TWIP steel was performed by tensile and reversed cyclic tests in a scanning electron microscopy (SEM) [46]. The authors found that detwinning did not start at the onset of stress reversal, but required a sufficient variation of the stress close to the absolute value of twin nucleation stress. In addition to the above detwinning results, few studies on deformation-induced detwinning of growth twins were also reported in literatures [47–50]. For example, in the electrodeposited nc Ni- 20 wt% Fe alloy, the pre-existing growth twins in grains smaller than 35 nm annihilated by detwinning after five turns of high pressure torsion (HPT) processing [47,48]. The authors believed that detwinning of growth twins was caused primarily by the dislocation-twin interactions and was more readily activated in nc grains due to the higher flow stresses. By in-situ nano-indentation studies on an epitaxially grown nano-twinned Cu foil, detwinning was revealed through a collective glide of the Shockley partial dislocations [51,52]. Unit dislocations usually dissociate at TBs to form partial dislocations which slip along TBs and result in a detwinning process [30,51,52].

Although both twinning and detwinning processes have been revealed as deformation mechanisms of fcc alloys with low SFEs, how to use them to obtain maximum strength-ductility combination has not been reported. In this work, brasses (Cu- 30 wt% Zn) with different grain sizes ranging from UFG to micro regions were fabricated by equal-channel-angular pressing (ECAP) combined with subsequent annealing. We achieved a maximum combination of tensile strength and ductility corresponding to a mean grain size of 3.8 μm. The microstructural evolutions and deformation mechanisms of all samples during tension were investigated by electron backscattered diffraction (EBSD) characterization in details. We revealed detwinning of pre-existing annealing twins at initial deformation stage and twinning at later deformation stage of which both result in the excellent strength-ductility combination.

2. Experimental materials and procedures

2.1. Sample preparation

As-received commercial Cu- 30 wt% Zn alloy rods with a diameter of 10 mm and a SFE of ~7 mJm^{-2} were first annealed at 600 °C for 1 h, and processed by ECAP using route Bc at 220 °C for three passes and then at 280 °C for two passes. During ECAP processing, the sample rod was rotated 90° after each pass, and detailed processing can be referred to our previous reports [36,37,53]. After ECAP, the deformed sample rods (designated as ECAPed sample) were annealed at 250 °C for 200 min, 400 °C for 40 min and 500 °C for 2 h under Ar atmosphere, which were designated as partially recrystallized (PR), fine-grained (FG) and coarse-grained (CG) samples, respectively.

2.2. Tensile testing

The tensile tests were performed using a custom-built computer controlled tensile test machine with a displacement resolution of 0.05 mm, a load resolution of 0.1 N and a constant strain rate of 10^{-3} s^{-1}. Flat dog-bone tensile specimens with a gauge cross-section of 1 × 0.5 mm and a length of 3 mm were electro-discharge machined from the sample rods. The tensile specimen axis was perpendicular with the direction of ECAP extrusion. Three tensile specimens were prepared for each sample rod to obtain repeatable experimental results.

2.3. Microstructure characterizations

Microstructural and grain orientation evolutions of Cu- 30 wt% Zn samples during tension were characterized by EBSD. First, the grip parts of the tensile specimens were used to analyze the initial undeformed microstructures. Second, the gauge areas of tensile specimens after the tensile deformed ~6% for the PR sample and ~10% for the FG and CG samples were selected for analysis of the early deformation stage. Third, the gauge parts of the fractured tensile specimens (~17% for the FG and ~23% for the CG samples) were used to analyze the later stage of deformation. The EBSD samples were mechanically polished first and then followed by electro-polishing using an electrolyte consisting of 85% phosphoric acid and 15% deionized water with a voltage of 2.1 V at room temperature. EBSD measurements were performed on Carl Zeiss Auriga focused ion beam scanning electron microscope equipped with an Oxford Instruments Aztec system (channel 5 software). EBSD scanning step size was chosen as 50 nm for all samples. The fracture surfaces were imaged by an FEI-XL30 SFEG SEM using a 20 kV beams. Transmission electron microscopy (TEM) observations were carried out on a FEI TECNAI 20 electron microscope operated at 200 kV. Cross-sectional TEM specimens were cut parallel to tensile direction (TD), polished to a thickness of ~30 μm, and then perforated by ion milling.
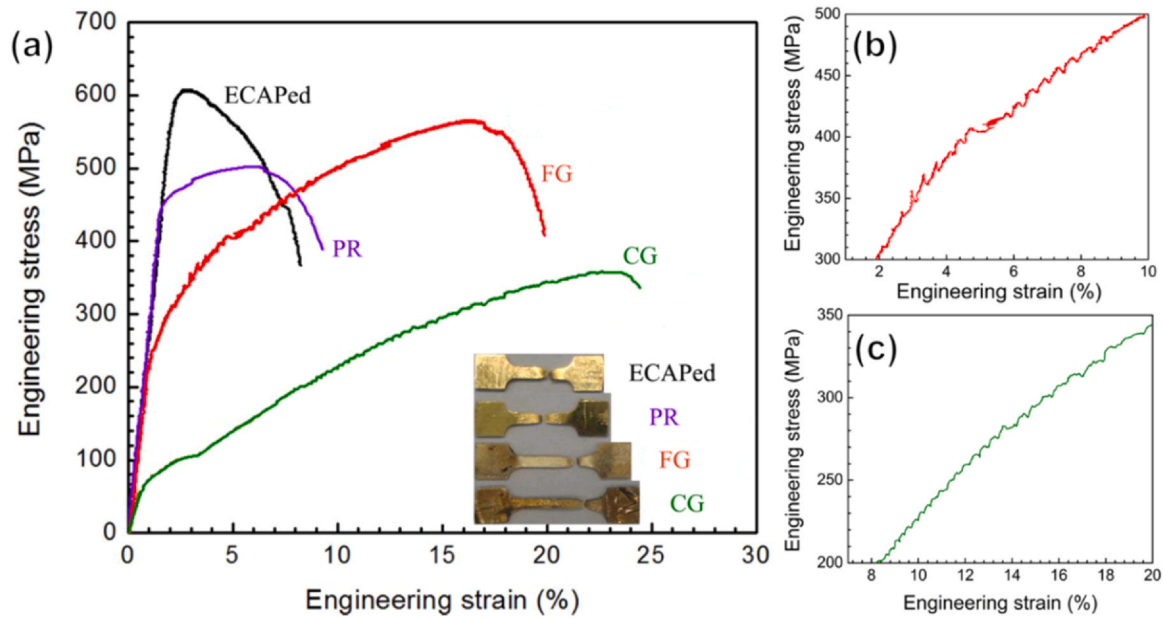
Fig. 1. (a) Tensile engineering stress-strain curves of the ECAPed, PR, FG and CG Cu- 30 wt% Zn samples. (b) and (c) are the corresponding serration behavior of the FG and CG samples, respectively. The inset in (a) shows the fractured tensile specimens.

3. Results

3.1. Mechanical properties

The representative engineering stress-strain curves of the ECAPed, PR, FG and CG Cu- 30 wt% Zn samples are compared in Fig. 1a. First, the CG sample has a YS of 50 MPa, a UTS of 350 MPa and a high ductility of 24%, as listed in Table 1. The ductility value is smaller than literature reported value (40%) because the small size of tensile specimen used here [54]. Our previous investigations revealed that the small cross section area of tensile specimens can reduce both uniform elongation and post necking part of the tensile curve due to the changes of fracture mechanisms from normal to shear fracture [55,56]. ECAP processing enhanced the YS up to 590 MPa but lower the tensile ductility down to 8%. Moreover, there is almost no uniform elongation and necking occurred immediately after yielding, resulting in the low ductility. After annealing, the strain hardening capacity was enhanced and the ductility rapidly increased. The PR sample annealed at 250 °C for 200 min has a reduced YS of 450 MPa and UTS of 500 MPa as well as ductility of approximate 9%. After annealing at 400 °C for 40 min, the YS of the FG sample was further decreased to 250 MPa. However, there exists a large strain hardening rate causing the tensile curve keeps going up and high UTS of 565 MPa as well as a high ductility of 20%, respectively. Notably, the ductility of the FG sample is close to the CG sample (24%). If we use the difference between UTS and YS to quantitatively characterize the strain hardening capability, then we found that the FG sample has an approximately similar or even slightly larger strain hardening capability (315 MPa) compared with the CG sample (300 MPa). This indicates that the FG sample has a
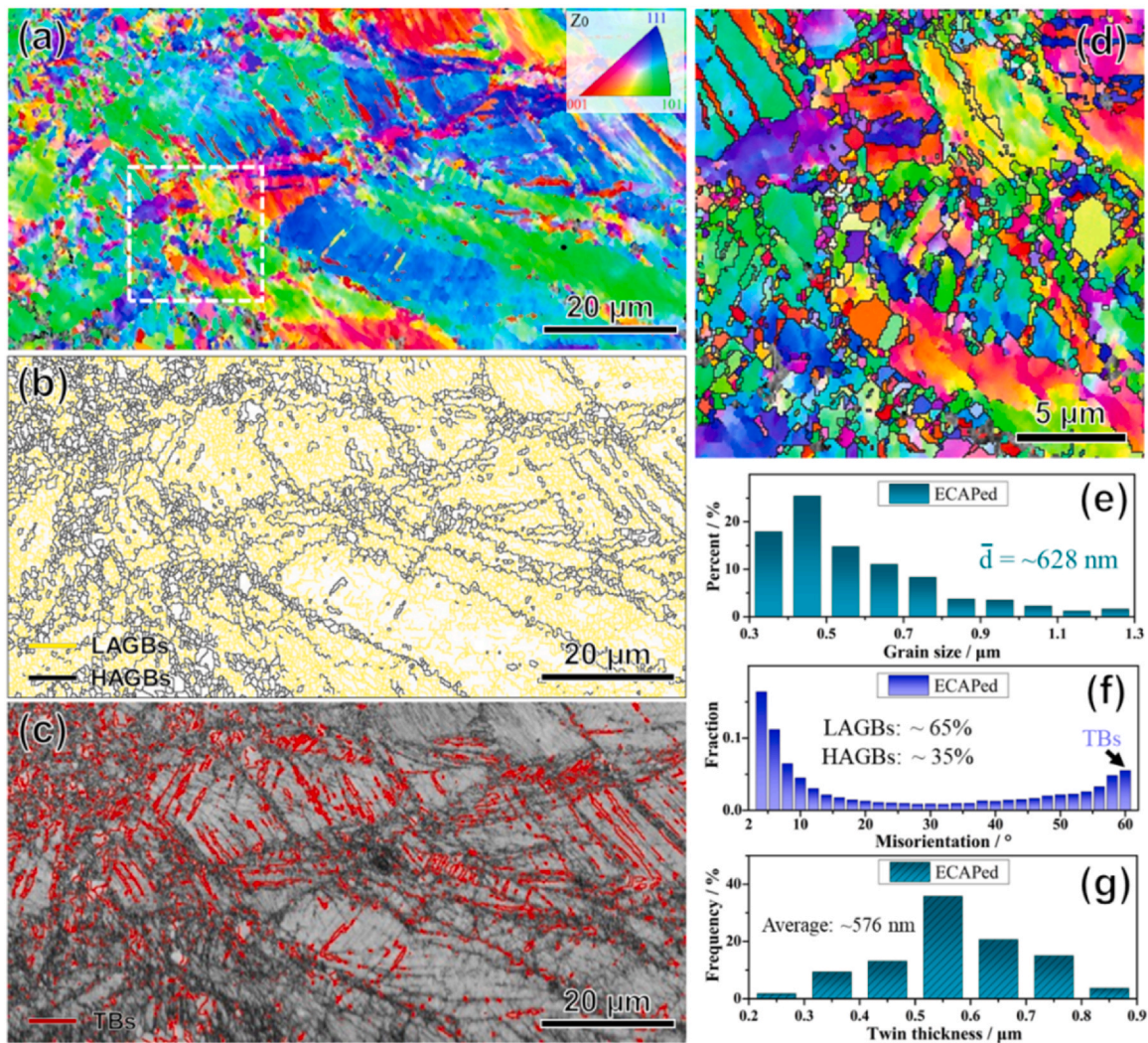
best combination of UTS and ductility due to its high strain hardening capacity. The strain hardening exponent n was usually used for evaluating strain hardening rate, of which values, simulated by Hollomon equation [57] are 0.41 for CG, 0.45 for FG and 0.15 for PR samples, further verifying the larger strain hardening capability of the FG sample compared with the CG sample.

Additionally, stress serrations are clearly visible on tensile curves of the FG and CG samples in Fig. 1a. The common causes of this phenomenon mainly include [58–60]: (1) the interaction between dislocation slip and solute atoms or nanoscale precipitates; (2) stress release caused by continuous twinning; (3) stress-induced phase transition. Magnified details of the tensile curves are presented in Fig. 1b and c. It is observed that compared with the CG sample the stress serrations in the FG sample occurred at the earlier strain stage and shows larger amplitude. For the FG sample, the serration behavior started at the tensile strain of 3% and the stress serration amplitude was ~10 MPa. With the tensile strain increased to 6%, the amplitude decreased and stabilized at ~5 MPa. The different serration behaviors in the FG sample were caused by initial detwinning and later twinning process, as revealed by EBSD analysis. For the CG sample, the serration behavior started at the tensile strain of 8% and the amplitude gradually increased and stabilized at ~2 MPa. The CG sample has a lager grain size and can store more dislocations under tension, resulting in dislocation slip at the earlier strain stage and twinning at later stage.

3.2. Initial microstructures before tensile tests

3.2.1. Initial microstructures of ECAPed sample

The EBSD results of the ECAPed Cu- 30 wt% Zn sample are shown in Fig. 2. The crystal orientation map with the color code (red, blue and green indicate grains have < 001 >, < 110 > and < 111 > directions parallel to the Z axis) shows a large number of randomly oriented grains in the ECAPed sample (Fig. 2a), indicating that there is no obvious fiber texture along the direction of ECAP extrusion. Boundaries with misorientation angles > 2° were considered as low-angle grain boundaries (LAGBs, 2°–15°) and high-angle grain boundaries (HAGBs, > 15°) including TBs at 60°, which are marked by yellow, black and red lines in Figs. 2b and 2c, respectively. From the EBSD GB map (Fig. 2b), the ECAPed sample is composed of plenty of

Table 1
Lists of yield strength (YS), ultimate tensile strength (UTS), strain hardening capability (the difference between UTS and YS, $\sigma_{UTS} - \sigma_{0.2}$), uniform elongation ε_{ue} and elongation to failure ε_{ef} of the ECAPed, PR, FG and CG Cu- 30 wt% Zn samples.

Samples	YS, MPa	UTS, MPa	$\sigma_{UTS} - \sigma_{0.2}$, MPa	ε_{ue}, %	ε_{ef}, %
ECAPed	590	605	15	3	8
PR	450	500	50	6	9
FG	250	565	315	17	20
CG	50	350	300	23	24

Fig. 2. EBSD maps of (a) crystal orientation, (b) grain boundary (GB) and (c) image quality with Σ3 twin boundary of the ECAPed Cu- 30 wt% Zn sample. The low- and high-angle grain boundaries (LAGBs: 2°–15°, HAGBs: > 15°) and twin boundaries (TBs: 60°) are marked by yellow, black and red lines, respectively. (d) The enlarged view of the square area in (a). (e–g) Histograms of grain size (e), GB misorientation angle (f) and the twin lamella thickness distributions (g) of the ECAPed sample. $\bar{d}$: average grain size. IPF color of Z_0 is applied.

UFG grains and a few lamellar micron grains. The color variations in each individual micro grain interior (Fig. 2a) indicate the large changes of interior misorientation caused by pronounced dislocation accumulation (yellow color in Fig. 2b) and deformation twinning (red lamellae in Fig. 2c). These results indicate that numerous dislocation cells and high-density dislocation entanglements as well as deformation twins were produced by ECAP processing. The submicrometer grains, easily seen from the enlarged view in Fig. 2d, are likely to form as a result of dynamic recrystallization during ECAP processing.

Fig. 2e is the statistical result of grain size and the average grain size is 628 nm. The GB misorientation angle distribution of the ECAPed sample is shown in Fig. 2 f, and the longitudinal coordinates "Fraction" in Fig. 2f is corresponding to the fraction of length. The ECAPed sample has dominant LAGBs (~65%). The HAGBs (~35%) also include ~7.4% TBs of the total GBs length. Moreover, the deformation twins have an average lamella thickness of 576 nm (Fig. 2 g). Therefore, the ECAPed sample was almost filled with deformed structures containing high-density dislocations, LAGBs, deformation twins, resulting in nearly null strain hardening capacity under tension.

3.2.2. Initial microstructures of PR sample

Fig. 3 shows the microstructures of the PR, FG and CG Cu- 30 wt % Zn samples. The PR sample has a mixed microstructure including recrystallization zone (white area in Fig. 3c) and deformation matrix (yellow area in Fig. 3c). The dashed area in Fig. 3c shows fully recrystallized coarse grains and UFG grains, which nucleated and grown inside the severely deformed grains. Plentiful annealing twins (marked by white arrows in Fig. 3e) with thicker twin lamellae were observed in randomly oriented recrystallized grains. The annealing growth twins are morphologically different from deformation twins (marked by black arrows in Fig. 3e). The former are stepped and parallel lamellar and the later are lenticular or wedge-shaped.

The non-recrystallized deformed matrix is still composed of high densities of dislocations and deformation twins (Fig. 3c and e). It is also verified from the statistical data in Figs. 4a and d that the fraction LAGBs is still high (~51%) and the average grain size is increased from 628 nm to 1.3 μm. The distributions of statistical lamellar twin thickness are shown in Fig. 4g, and the average lamella thickness of the PR sample is ~503 nm.
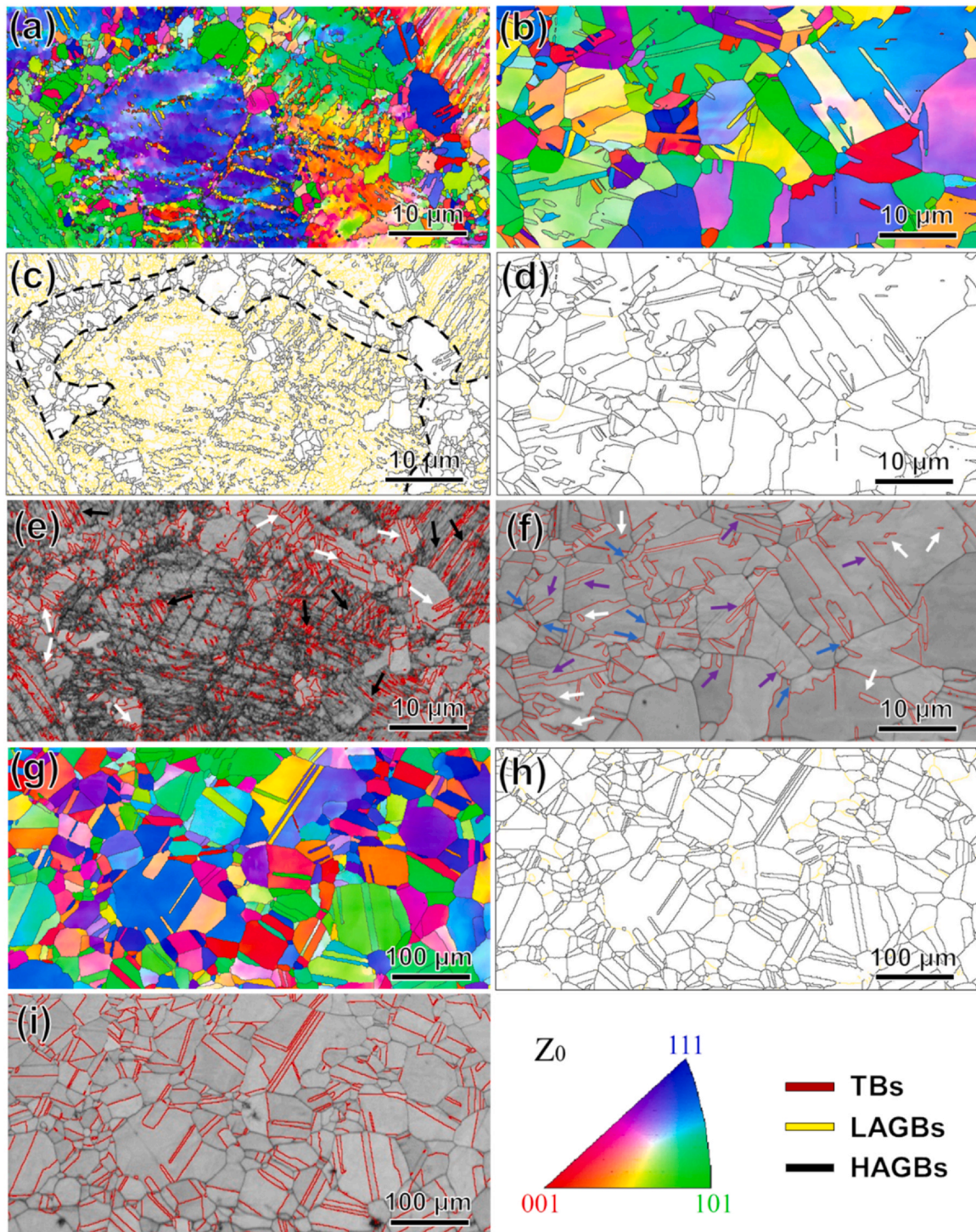
Fig. 3. EBSD crystal orientation, GB and image quality maps of (a, c, e) PR, (b, d, f) FG and (g, h, i) CG Cu- 30 wt% Zn samples. The LAGBs, HAGBs and TBs are marked by yellow, black and red lines, respectively. IPF color of Z_0 is applied. The dashed area in (c) shows the recrystallized area. The annealing twins were pointed by white arrows and the deformation twins were pointed by black arrows in (e). The corner, isolated and stepped annealing twins were pointed by blue, white and purple arrows in (f), respectively.

3.2.3. Initial microstructures of FG and CG samples

As shown in Fig. 3b and g, both FG and CG samples consist of randomly oriented equiaxed micron-sized grains with HAGBs. Almost uniform color contour in individual grain interior indicates slight changes of interior misorientation and lower dislocation accumulation as well as full recrystallization. The FG and CG samples have the average grain sizes of 3.8 μm and 30.6 μm, respectively (Fig. 4b, c).

As shown in Fig. 3f and i, both FG and CG samples have high densities of annealing twins inside the recrystallized grains. For the FG sample, the average lamella thickness is 481 nm, as shown in Fig. 4h. The statistical distributions of lamellar twin thickness in Fig. 4h also revealed that most annealing twins have thickness smaller than 1 μm, while a small amount of twins have a thickness greater than 1 μm. It is worth noting that twins with thickness smaller than 50 nm cannot be identified by the EBSD technique due
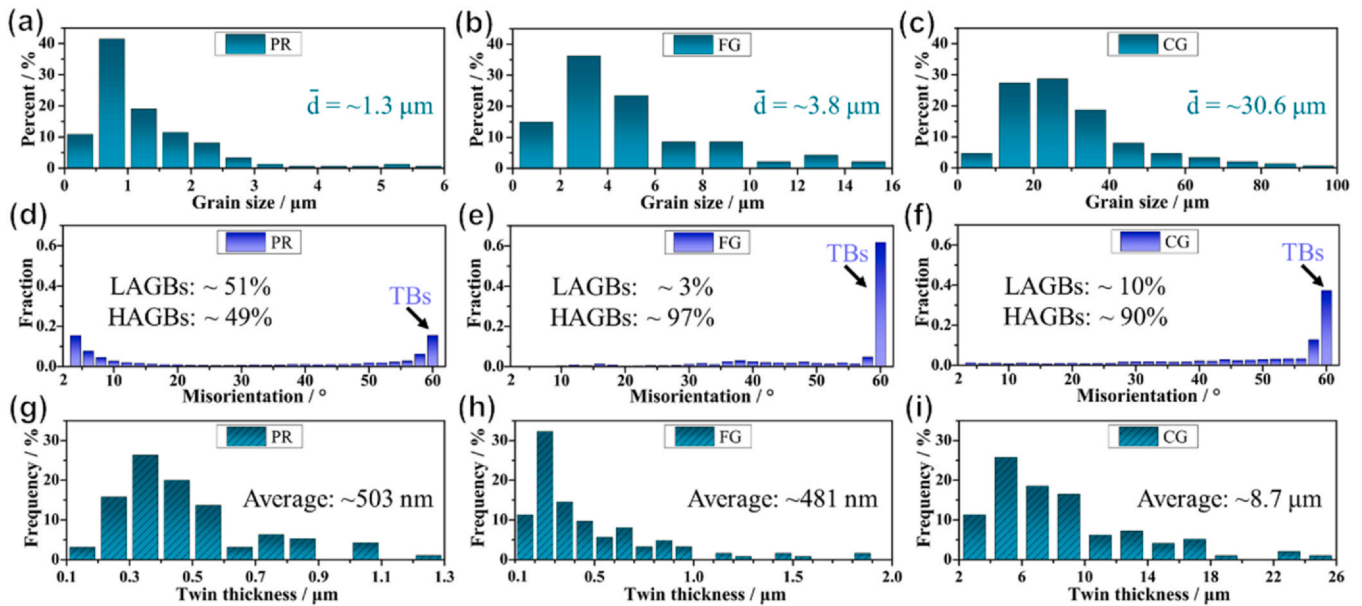
Fig. 4. Distributions of grain size, GB misorientation angle and lamellar twin thickness of (a, d, g) PR, (b, e, h) FG and (c, f, i) CG Cu-30%Zn samples. $\bar{d}$: average grain size.

to its limited resolution. Therefore, we also performed TEM observation in order to supplement EBSD information. The average twin lamella thickness of the FG sample, counted from TEM images (Fig. 10a), is 315 nm, smaller than the EBSD results. This is because there is small amount of annealing twins (about 10%) with thickness smaller than 50 nm. Nevertheless, the results of EBSD statistics are still comparable due to the same error. In addition, Fig. 3f also revealed most annealing twins nucleated at HAGBs but did not grow fully to the opposite HAGBs, terminated at grain interiors and retained growth steps, as marked by purple arrows in Fig. 3f. The stepped twins are also found in TEM image (Fig. 10a). The typical coherent twin relationship was verified by the selected-area electron diffraction (SAED) pattern in Fig. 10b. Some annealing twins pointed by white arrows in Fig. 3 f are completely isolated within the grains indicating they nucleated at grain interiors. Also, some corner twins pointed by blue arrows in Fig. 3f nucleated at triple GB junctions. For the CG sample, the wide and straight twin lamellae can be seen in Fig. 3i, morphologically different from those in the FG sample. These twins usually traversed the grains and part of them terminated at the interior. Due to more fully annealing, twins in the CG sample grew thicker with an average lamella thickness of 8.7 μm.

The distributions of GB misorientation angles of the FG and CG samples are shown in Fig. 4e–f, respectively. The peak at 60° is corresponding to Σ3 coincident-site lattice TBs. The FG sample has ~97% HAGBs and ~62% TBs. The CG sample has the similar HAGBs fraction of ~90%, but lower TBs fraction of ~37%. With further annealing, the proportion of TBs dramatically decreased due to the grain growth. Considering that TB is a kind of HAGB with specific angle, the ratio of TBs and HAGBs length was calculated and designated as T/H. The T/H in the FG sample is ~63.9%, much higher than that in CG sample (~41.1%), indicating that the FG sample has higher density of annealing twins.

3.2.4. Local misorientation maps of initial samples

The local misorientation maps of the ECAPed, PR, FG and CG Cu-30%Zn samples are shown in Fig. 5. Blue regions represent smaller

local misorientation and have lower density of GNDs. Conversely, green and red regions have higher stored strain energy. The ECAPed sample has high GNDs density and stores large plastic strain energy (Fig. 5a). These stored energy facilitated dislocations migration, rearrangement, and annihilation during annealing. Kernel average misorientation (KAM) value of the ECAPed sample is 1.66°, as shown in Fig. 5e. The PR sample shows partial blue region and green region, as shown in Fig. 5b. The blue regions are recrystallized grain areas and the green regions are relative to deformed areas, consistent with Fig. 3a. Intuitively, the KAM value of the PR sample in Fig. 5e shows a bimodal distribution due to the partially recrystallized microstructures with an average KAM value of 1.19°. The FG and CG samples have fully recrystallized after annealing and have larger KAM values in the area close to conventional HAGBs and TBs and comparatively smaller KAM values in the interior of the grains. The average KAM values of FG and CG are 0.22° and 0.19°, respectively.

The GNDs density has linear relation with the average KAM value and can be calculated by the formula from the strain gradient theory by Gao [61] and Kubin [62]:

$$\rho = \frac{2\theta^{KAM}}{ub} \tag{1}$$

where ρ is the GNDs density; u is the unit length, equal to twice the step size, which is 50 nm, used in EBSD acquisition; b is the Burgers vector (0.261 nm in use); θ^{KAM} is the average KAM value. The calculated GNDs densities are 2.2×10^{15} m^{-2} for the ECAPed, 1.6×10^{15} m^{-2} for the PR, 3×10^{14} m^{-2} for the FG and 2.6×10^{14} m^{-2} for the CG samples, as listed in Table 2.

3.3. Microstructural evolutions during tensile deformation

Microstructural evolutions of the PR, FG and CG Cu- 30 wt% Zn samples during tensile testing were performed by EBSD. Specifically, deformation mechanisms in low strain stage (~6% for PR, ~10% for FG and CG) and high strain stage (~17% for FG and ~23% for CG) were analyzed.
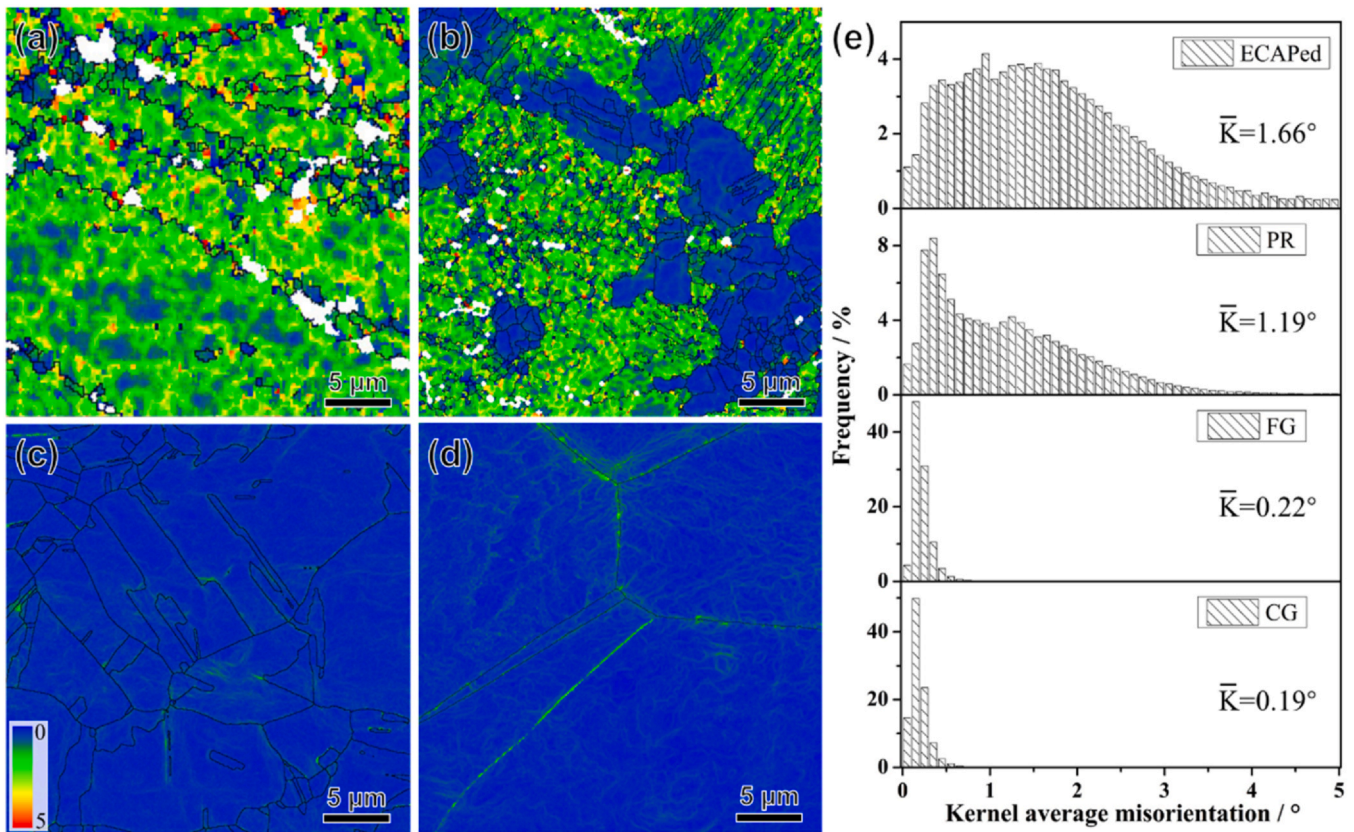
Fig. 5. The local misorientation maps of (a) ECAPed, (b) PR, (c) FG and (d) CG Cu- 30 wt% Zn samples. The inset in (c) is the rainbow color bar (blue to red represent low to high misorientation). (e) The corresponding Kernel average misorientation (KAM) value distributions of the four samples. $\bar{K}$: average KAM value.

Table 2

Lists of HAGBs fraction (FHAGBs), average twin lamella thickness ($\bar{T}$), average grain size ($\bar{d}$) and the density of GNDs (ρ) of the ECAPed, PR, FG and CG Cu- 30 wt% Zn samples from EBSD data.

| Samples	FHAGBs (%)	$\bar{T}$ (μm)	$\bar{d}$ (μm)	ρ (m^{-2})
ECAPed	35	0.576	0.628	2.2×10^{15}
PR	49	0.503	1.3	1.6×10^{15}
FG	97	0.481	3.8	3×10^{14}
CG	90	8.7	30.6	2.6×10^{14}

3.3.1. Deformation at low strain stage

The microstructures of the PR Cu-30%Zn sample with 6% tension are shown in Fig. 6. The double sided arrow indicates TD. Due to the existed deformed structure, further plastic deformation hardly occurred in these areas during tensile test. In the recrystallized area, delineated by black dotted line in Fig. 6b, grains underwent obvious plastic deformation. IPF colors of these grain interiors have changed significantly and there are a small amount of LAGBs (Fig. 6a, b). As a result, the LAGBs fraction was increased from ~51% for the undeformed PR sample to ~55% after tension (Fig. 6e). The deformation of the recrystallized grains can be further verified by the local misorientation map, as shown in Fig. 6d, which exhibited green color and revealed high-density dislocations in these grains. The average KAM value increased from 1.19° (undeformed PR sample) to 1.52° after 6% tension (Fig. 6f). The initial deformation twin lamellae are retained in deformed matrix after tension (Fig. 6c), and no evident further twinning was observed in the recrystallized grains due to low tensile strain. These observations indicate the main deformation

mechanism of the PR Cu-30%Zn sample is dislocation slip in recrystallized areas.

Fig. 7 shows the crystal orientation, grain boundary and image quality maps of the FG and CG Cu- 30 wt% Zn samples after 10% tension. It is apparent that all grains are elongated along TD, as observed from all maps. Pronounced orientation variations and a large number of LAGBs can be observed inside nearly all of the grains (Fig. 7c, d), due to numerous dislocations accumulation and entanglement. The LAGBs fraction of the FG and CG samples increased from ~3% to ~53% and ~10% to ~72%, respectively. Furthermore, except many parallel slip lines produced in all grains (marked by green arrows), multiple slip systems were even activated in certain individual grain, as marked by black lines in Fig. 7f. Moreover, most stepped and isolated ultrafine lamellar growth twins in the FG sample (marked by blue, purple and white arrows in Fig. 3f) annihilated by detwinning under 10% tension causing a significant decrease in TB fraction (Fig. 7g, h). The length fraction of TBs decreased sharply from ~62% to ~5.7% for the FG sample (Fig. 7g, h). In addition, the original micro-sized annealing twins (T1 and T2 in the FG sample; T3-T5 in the CG sample) also gradually deviate from their twin relationship, resulting in the disappearance of TBs (Fig. 7e, f). The TBs length fraction of the CG sample decreased sharply from ~37% to ~3.5%. The ultrafine twin lamellae annihilated via detwinning and the micro twin lamellae via conversion of TBs into conventional HAGBs of which mechanisms will be discussed in Section 4 below.

Except above mentioned numerous longitudinal slip bands and detwinning, a few deformation twins (pointed by black arrows in
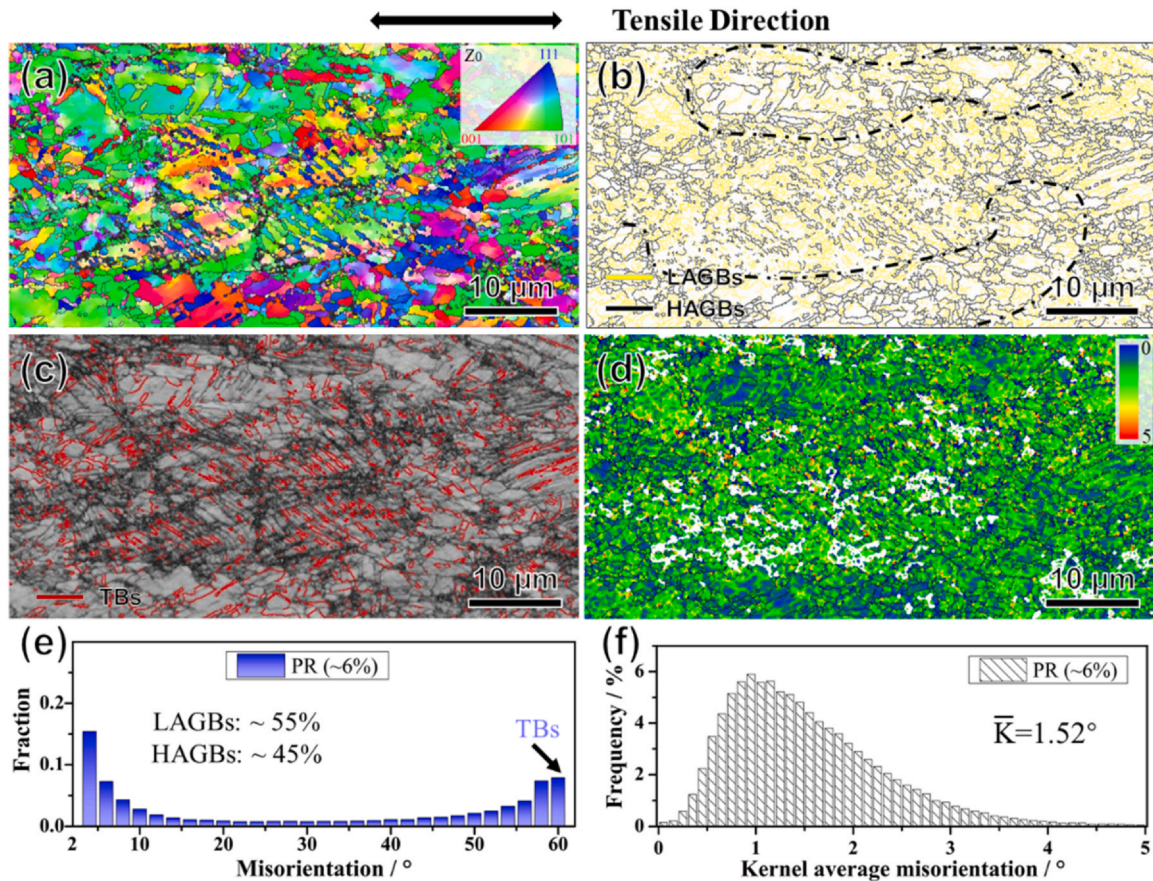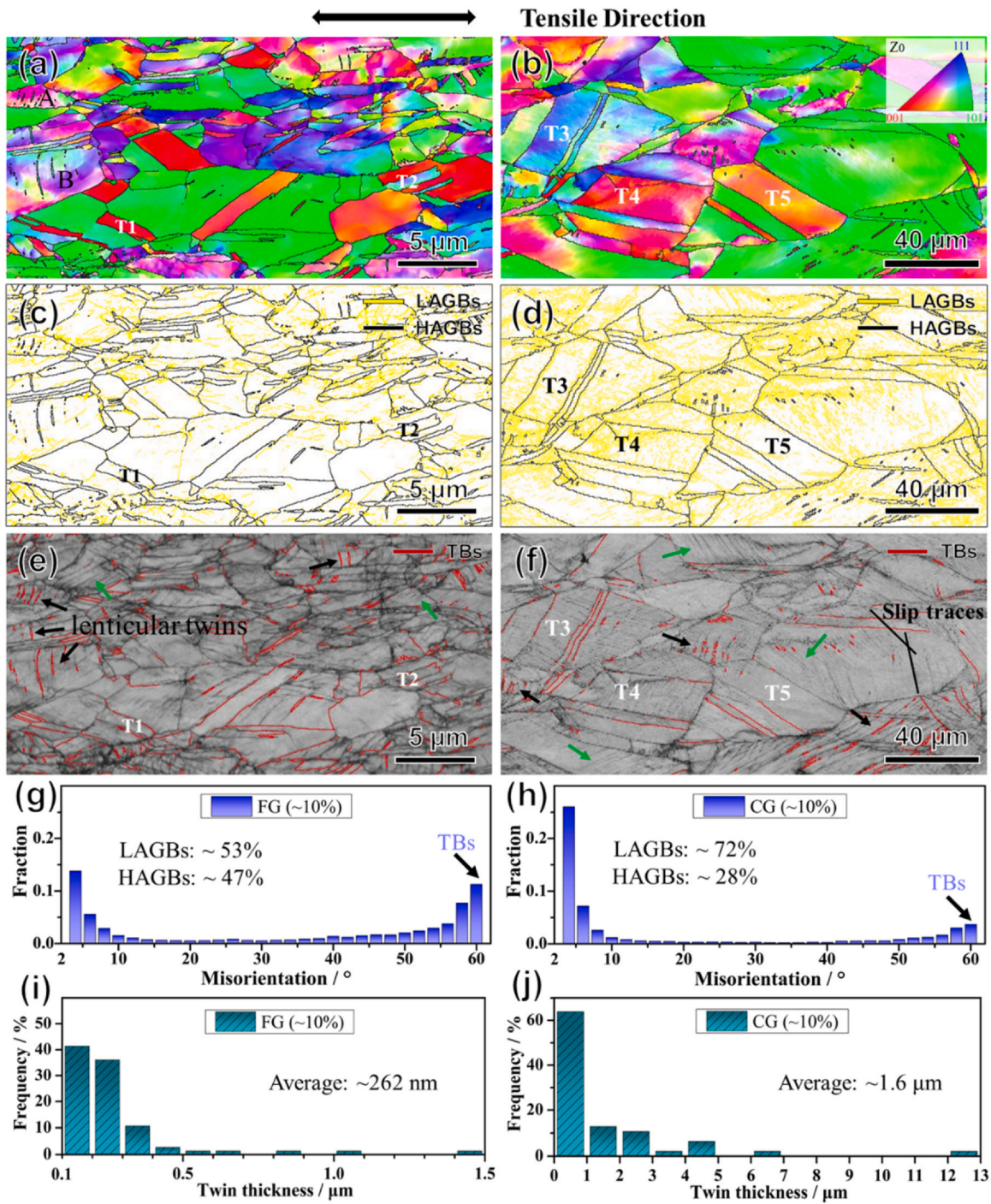
Fig. 6. (a) EBSD crystal orientation, (b) GB, (c) image quality and (d) local misorientation maps of the PR Cu-30%Zn sample after 6% tension. Distributions of (e) GB misorientation angle and (f) KAM value. IPF color of Z0 is applied.

Fig. 7e, f) were also produced in grains with favorable orientation. These deformation twins are thin, lenticular and parallel to each other, different from the morphologies of pre-existing annealing twins. From the distributions of lamellar twin thickness in Fig. 7i and j, one can see that high fraction of thinner deformation twin lamellae were produced and caused the average thickness decreased from initial 481–262 nm for the FG sample and from 8.7 μm to 1.6 μm for the CG sample, respectively. Careful observation reveals that deformation twinning occurred in grains with high orientation gradients, like grains A and B in Fig. 7a. Grains with high orientation gradients mean these parent grains have high dislocation densities and localized stress concentrations. Moreover, these deformation twins nucleated at HAGBs and grew into the grain interior, nearly perpendicular to TD. The above deformation twins with smaller thickness than annealing twins was further verified by TEM observation. As shown in Fig. 10c, high-density nanoscale twin bundles emit from the grain boundary and penetrate the grain. The average lamellar thickness of these deformation nanoscale twins is 26 nm, which were unidentifiable by EBSD. It was widely reported that with increasing grain size the critical stress required for twinning decreases and deformation induced-twinning becomes easier in coarse grained metal and alloys [33]. However, we observed twinning tends to occur in some small grains here, such as grain A in Fig. 7a, because

of the larger stress concentration in small grains than that in large grains. Another important influence factor of grain orientation may play a key role in governing twinning behavior, which will be discussed in the next section. Therefore, for the FG sample, detwinning of annealing twins, dislocation glide, slightly twinning are the main deformation mechanism at early strain stage.

Fig. 8 shows the local misorientation maps for the FG and CG samples after 10% tension. The obviously inhomogeneous deformation at microscale occurred in the FG and CG samples. For the FG sample (Fig. 8a), the HAGB neighboring areas were severely deformed, as revealed by the green color with high density of dislocations, and grain interiors were almost not deformed, as shown by the blue color with low dislocation densities. This inhomogeneous plastic deformation is mainly resulted from the presences of HAGBs and grain orientation. The CG sample also has high density dislocation near HAGBs (Fig. 8b). Moreover, the green lines inside grains are slip lines with a large accumulation of dislocations, which can also be observed in the FG and CG samples. From the corresponding KAM value distribution (Fig. 8c), the CG sample has a larger average KAM value of 1.45° compared to the FG sample with 1.16°, indicating the CG sample stored more dislocations at low strain stage. The GNDs densities were calculated from the above Eq. (1) and are 1.5×10^{15} m^{-2} for FG and 1.9×10^{15} m^{-2} for CG samples, respectively.

Fig. 7. EBSD crystal orientation, GB and image quality maps of (a, c, e) FG and (b, d, f) CG Cu- 30 wt% Zn samples after 10% tension. (g-j) The corresponding distributions of GB misorientation angle and lamellar twin thickness of (g, i) FG and (h, j) CG samples. Annealing twins with micron-sized thickness were marked as T1-T5 and grains with high orientation gradients were marked as A and B in the FG sample. The lenticular deformation twins and slip bands in both samples were pointed by black and green arrows in the image. IPF color of Z_0 is applied.

3.3.2. Deformation at high strain stage

Fig. 9 shows the crystal orientation, grain boundary and image quality maps after 17% tension for the FG and 23% for the CG Cu-30 wt% Zn samples. The low indexing rate illustrates severe plastic strain occurred and the dislocation density increased drastically. Besides producing high-density dislocations, numerous deformation twins were also produced in both samples.

For the FG sample, a mass of deformation twins existed in almost all grains (Fig. 9c). These deformation twins are different from pre-existing annealing twins in Fig. 3 f, which possess thinner lamella thickness with an average value of 240 nm and were emitted from HAGBs. From TEM image (Fig. 10d), the grains were elongated and most have high-density nanoscale twin bundles with an average lamellar thickness of 43 nm. As shown in Fig. 9h, the lamella
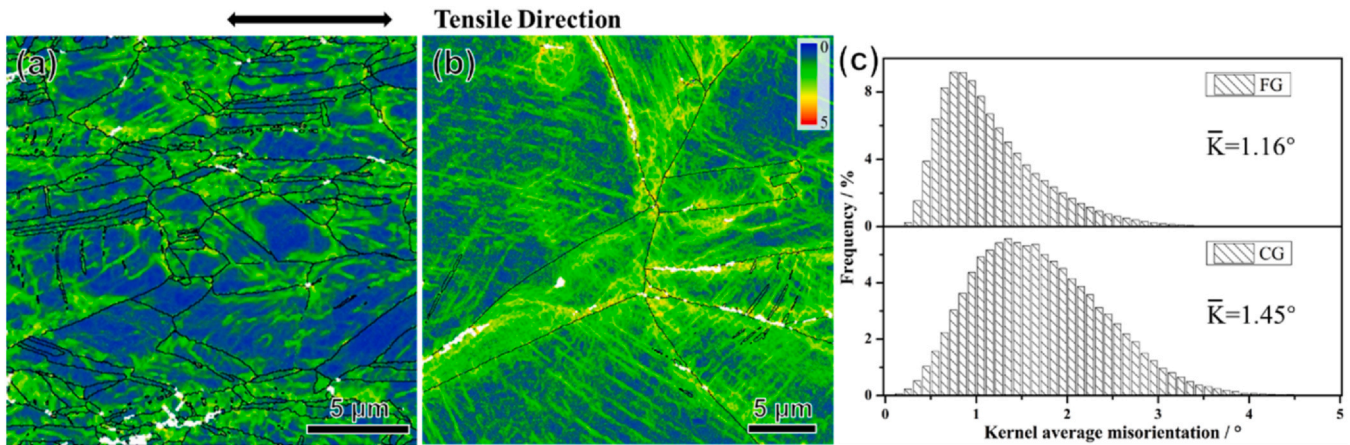
Fig. 8. The local misorientation maps of (a) FG and (b) CG Cu- 30 wt% Zn samples after 10% tension. (c) The corresponding KAM value distributions of both samples.

thickness of all twins are smaller than 500 nm indicating the TBs of the initial micro-sized annealing twins completely disappeared. Certainly, some residues of annealing twins with micron-sized lamella thickness can be observed, as marked by the black rectangular box in Fig. 9a and c. The TB fraction was further increased from ~5.7% (10% tensile strain) to ~8.1% (17% tension) verifying the occurrence of twinning (Table 3). Moreover, there are plentiful slip lines intersecting with the twinning plane, produced by dislocation motion (black lines in Fig. 9c). As listed in Table 3, the HAGBs fraction was further decreased from ~47% (10% tension) to ~33% (17% tension). It should be noted that a few grains have no deformation twins, like grains C and D in Fig. 9a–c. Both grains are micron-sized and accumulated high density of dislocations. This implies grain orientation plays an important role for twinning in Cu- 30 wt% Zn alloy. The detailed analysis of grain orientation governing twinning activity will be discussed in next section.

The CG sample with triple GB junction after high strain tension is shown in Fig. 9d–f. The lathy deformation twins are parallel with each other, similar to the FG sample. The CG sample has an average twin lamella thickness of 218 nm (Fig. 9h). Numerous slip lines (black lines in Fig. 9f) separate the deformation twins to a series of slices suggesting that intense interaction between dislocations and deformation twins occurred.

3.4. Fracture morphologies

To further understand the relationship between microstructures and mechanical properties, SEM observations were performed on the fracture surface morphology. Fig. 11 shows SEM images of the macro- and micro-scale fracture surfaces of the ECAPed, FG and CG Cu- 30 wt% Zn samples, respectively. The three samples fractured in a ductile manner, as evidenced by the homogeneously distributed honeycomb-like dimples and a large area reduction of fracture surface.

4. Discussion

4.1. Microstructure-property relationship

From the above results, the ECAPed Cu- 30 wt% Zn underwent severe plastic deformation and consisted of numerous deformation structures containing high density of dislocations, LAGBs and deformation twins. In addition, a large number of equiaxed ultrafine grains with an average grain size of about 600 nm existed in the ECAPed sample due to recrystallization during ECAP. High densities of lattice defects containing conventional HAGBs, TBs and dislocation substructures result in the high YS close to 600 MPa, low ductility and poor strain hardening capacity with the $\sigma_{UTS \text{-} \sigma_{0.2}}$ value of only 15 MPa.

After annealing, the ductility was enhanced gradually and the strength simultaneously decreased due to the recovery of defects and the recrystallization. The PR sample is composed of deformed (hard domains) and recrystallized areas (soft domains) due to partial recrystallization. It was widely reported that pronounced synergistic strengthening effect were produced between hard and soft domains and an extra strain hardening was obtained in heterostructured materials [63–66]. However, our PR sample has no excellent strain hardening capacity and the $\sigma_{UTS \text{-} \sigma_{0.2}}$ value is only 50 MPa, causing a small improvement of ductility compared to the ECAPed sample. From Fig. 5b, the apparent strain partitioning exists between hard and soft domains, which may maximize HDI hardening effect [66,67]. However, the outstanding HDI hardening did not improve the tensile curve of the PR sample. This might be explained as the strength difference between hard and soft domains may be too large so that the hard domain may not plastically deform. This can be further confirmed from Fig. 6d that the KAM value of hard domains almost has no change after tensile deformation. Strain localization and stress concentration may occur at the interface of hard and soft domains, leading to the failure fracture at the interface.

For the fully recrystallized FG and CG samples, both are composed of micron-sized grains with high density of annealing twins. Due to the difference between annealing time and temperature, the annealing twin lamella thicknesses and morphologies are quite different (Fig. 3f, i). The annealing twins in the CG sample grew into micron-sized and straight lamellae as the grains attained full growth. In contrast, most annealing twins in the FG sample are immature twins with ultrafine lamellae, including isolated and stepped twins. With the development of the annealing process, the ductility was improved and the YS decreased. It is worth noting that the FG sample has analogously good ductility and more outstanding strain hardening capacity, compared to the CG sample. The values of $\sigma_{UTS \text{-} \sigma_{0.2}}$ are 315 MPa for the FG sample and 300 MPa for the CG sample (Table 1), respectively. From the comparison of our results with literature data [19–21,68–70] in Fig. 12, it can be found that the
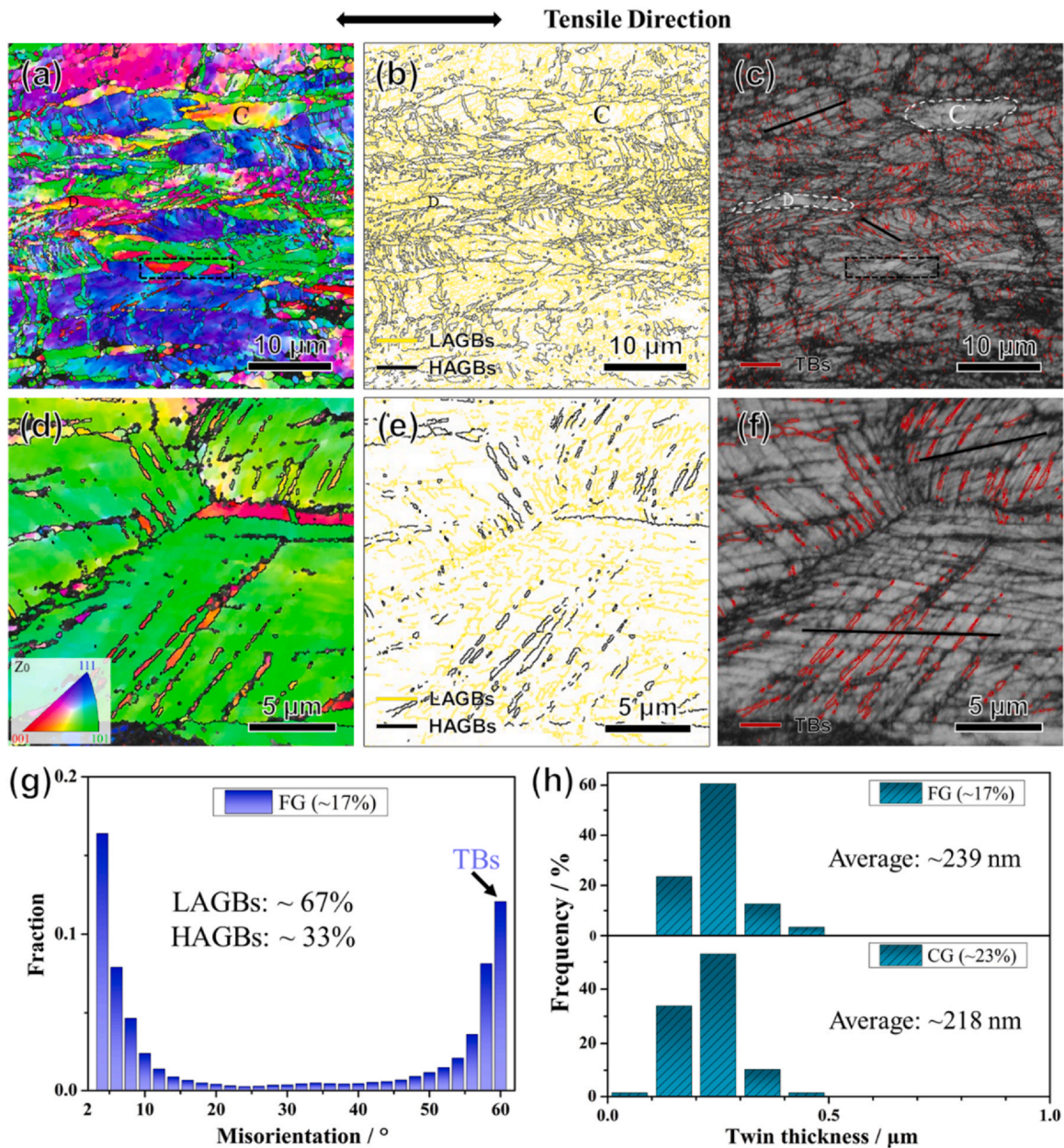
Fig. 9. EBSD crystal orientation, GB and image quality maps of (a-c) FG and (d-f) CG Cu- 30 wt% Zn samples after 17% and 23% tension, respectively. (g) The GB misorientation angle distribution of the FG sample. (h) The corresponding distributions of lamellar twin thickness of the FG and CG samples. Grains C and D in the FG sample are free of twins. Black lines in (c) and (f) are slip lines. IPF color of Z_0 is applied.

values of σ_{UTS} - $\sigma_{0.2}$ of metals and alloys with high SFEs are generally smaller than 200 MPa, and decrease with the decreased grain size (>1 µm). For Cu- 30 wt% Zn alloys in this work, the values of σ_{UTS} - $\sigma_{0.2}$ of the FG and CG samples are significantly larger. Interestingly, with grain size decrease from the CG to the FG, the value of σ_{UTS} - $\sigma_{0.2}$ increases. The excellent strain hardening capacity of the FG Cu-30% Zn may be mainly attributed to the following four factors. Firstly, high fraction of HAGBs including a large number of pre-existing TBs (Figs. 3f and 4e) can be effective to block and accumulate the dislocations. Especially the dispersed ultrafine isolated twin lamellae, as shown in Fig. 3f, can significantly improve the flow stress by

accumulating numerous dislocations. Secondly, low dislocation densities, i.e. high dislocation storage capacity, can accumulate more dislocation inside grains. Thirdly, deformation-induced detwinning of ultrafine annealing twin lamellae (< 1 µm) can effectively enhance the ductility by means of promoting the blocked dislocations at the TBs to further slip. Finally, pronounced deformation twinning occurred in almost all grains and high densities of deformation twins were produced. Dynamic strain hardening by the interaction of dislocations and TBs were produced due to reducing the dislocation mean free path.

Meanwhile, the FG sample has the higher YS of 250 MPa compared with the CG sample (50 MPa), as listed in Table 1. For the FG
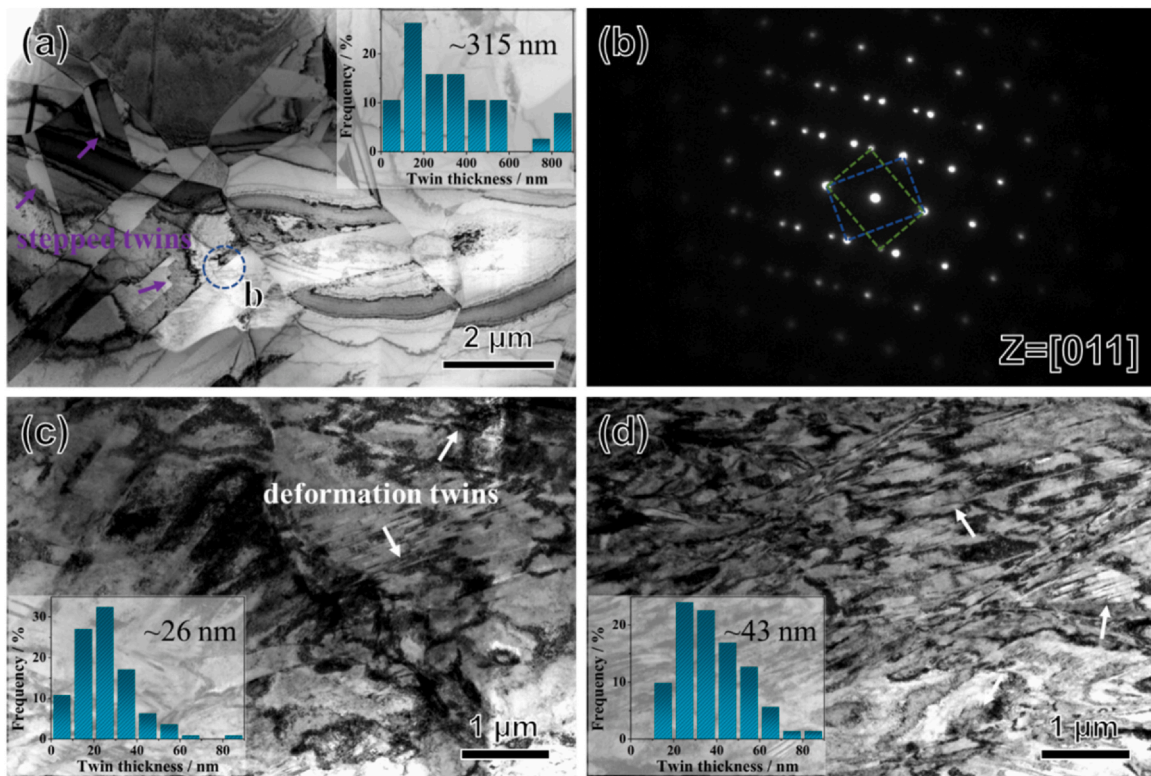
Fig. 10. Bright field TEM images of the FG samples (a) before tension, (c) after 10% and (d) 17% tension. The insets are the corresponding distributions of lamellar twin thickness. (b) The SAED pattern of the circled area in (a). The stepped annealing twins were pointed by purple arrows in (a), and the deformation twins were pointed by white arrows in (c) and (d).

Table 3
Lists of the values of length proportion of HAGBs, TBs and T/H and average twin lamella thickness ($\bar{T}$) in the FG Cu- 30 wt% Zn sample at different strains.

	0	~10%	~17%
FHAGBs(%)	96.7	47.2	32.9
FTBs(%)	60.8	5.7	8.1
FT/H(%)	62.9	12.1	24.6
$\bar{T}$ (nm) (EBSD)	481	262	239
$\bar{T}$ (nm) (TEM)	315	26	43

sample with smaller grain size, in addition to GB strengthening, the higher YS may be attributed to the numerous ultrafine annealing twin lamellae. These pre-existing ultrafine twins dispersing inside the grains can increase the critical stress for dislocation slip, thereby increasing the YS.

4.2. Deformation-induced detwinning of annealing twins

Annealing introduced high density of growth twins inside the grains of the FG and CG samples (Fig. 3). Different from the CG sample with micro-sized twin lamellae, the FG sample also contains numerous submicron-sized counterparts (Fig. 4h, i). For the CG sample, the micro-sized twin lamellae with thicknesses larger than 2 µm and even several tens of micrometers gradually disappeared by converting TBs into conventional HAGBs under tension. However, the annealing twins in the FG sample annihilated in various ways under tension, as discussed as below.

The visualized evolutions of twin lamella thickness and length proportion of HAGBs, TBs and T/H of the FG sample are shown in Fig. 13 and the corresponding quantitative data are listed in Table 3. With the applied strain increased, the fraction of HAGBs monotonically decreased, and the fraction of TBs first dramatically decreased and then slightly increased. Considering that the total HAGBs length is closely related to the length of TBs, which is a kind of HAGBs with specific angle, T/H was calculated. The values of T/H first dramatically decreased and then significantly increased with the increased strain. It indicates that with the increased strain the total length of TBs in the FG sample first decreased due to the detwinning process and the conversion of TBs into conventional HAGBs, and then increased due to the deformation twinning process.

Deformation-induced detwinning of annealing twins in the FG sample may be related to a collective glide of the Shockley partial dislocations along TBs. When the slip direction of the Shockley partial dislocations is in opposite direction of the twinning direction, detwinning occurs accompanying with decrease of the twin lamella thickness [30,71]. In order to comprehend the interaction of dislocations with TBs in the FG sample under tension, detwinning process is illustrated in Fig. 14. As the tensile stress increased at the initial stage of deformation, for the immature annealing twin that has a thin lamella thickness (< 1 µm) with a step or terminated inside of grains resulting from incomplete growth, deformation-induced detwinning process is easily to be activated by shrinking the twin partials at the step or the end of half twins. In addition, when full dislocations start to slip to and pile up at the TBs, as shown in
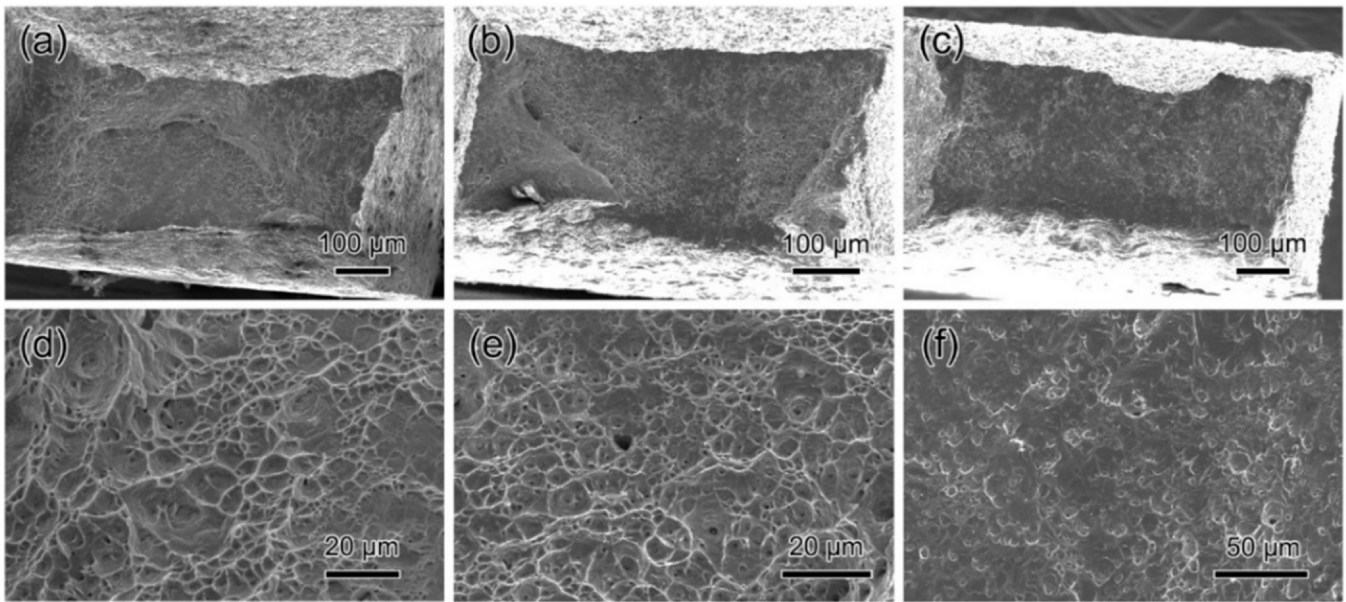
Fig. 11. SEM images of fracture surfaces of (a, d) ECAPed, (b, e) FG and (c, f) CG Cu- 30 wt% Zn samples: (a-c) Low magnification; (d-f) High magnification.
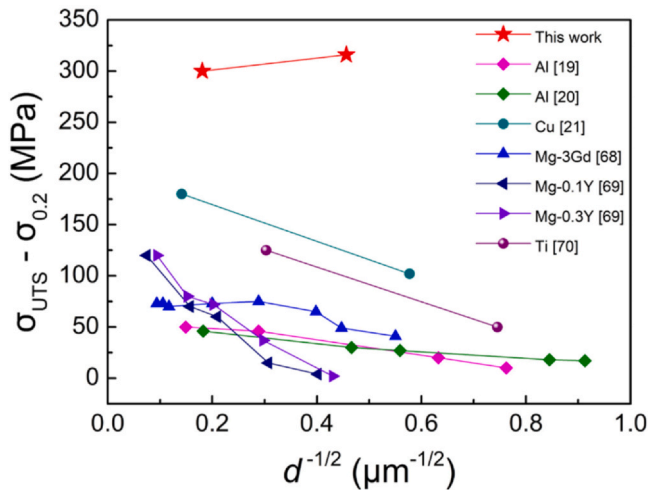

Fig. 12. Literature review for relations of grain size and strain hardening capacity of metals and alloys with high SFEs [19–21,68–70] and Cu- 30 wt% Zn alloys in this work. Grain sizes of all statistical materials are larger than 1 μm. σ_{UTS} - $\sigma_{0.2}$ is the difference in values between ultimate tensile strength (σ_{UTS}) and yield strength ($\sigma_{0.2}$).
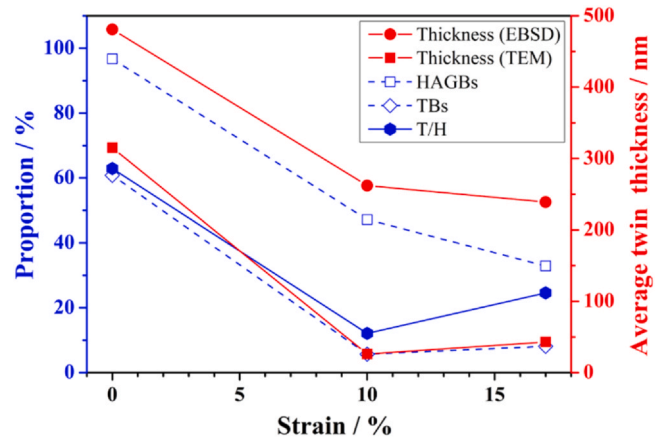

Fig. 13. The evolutions of length proportion of HAGBs, TBs and T/H and average twin lamella thickness in the FG Cu- 30 wt% Zn sample under uniaxial tension. T/H is the fraction of TBs in the total HAGBs length.

Fig. 14b, the full dislocation dissociates into two Shockley partials, and one partial glides to the right along the TB under the increased applied stress, resulting in the reduction of twin thickness (Fig. 14c). The other one partial glides to and accumulated at the new TB, and then dissociates into a stair-rod dislocation and a new partial. The new partial glides to the left along the TB. Meanwhile, the stair-rod dislocation dissociates into two new Shockley partials and repeats the above process.

4.3. Effect of grain orientation on deformation twinning

As an important deformation mechanism, deformation twinning plays a key role to coordinate plastic deformation in materials with low SFEs. Generally, metals and alloys with low SFEs have the excellent strain hardening capacity and uniform elongation resulting from abundantly produced deformation twins. For the FG and CG Cu- 30 wt% Zn samples in this study, the excellent strain hardening capacity is reflected by σ_{UTS} - $\sigma_{0.2}$, as shown in Fig. 12.

It was widely reported that the effect of grain size plays an important role on deformation twinning under plastic deformation [34–40,72,73]. Nevertheless, the effect of grain orientation on deformation twinning, especially for Cu- 30 wt% Zn alloys during uniaxial tensile deformation, was rarely reported. As is well-known, the pronounced fiber textures, <100> // TD and <111> // TD, may be produced in fcc metals and alloys during uniaxial tensile deformation [73,74]. Differing from the <100> // TD and <111> // TD oriented grains, grains with <110> // TD orientation are less stable and inclined to rotate towards orientations in favor of dislocation slip during tensile deformation [75,76]. Fig. 15a shows the evolution of fiber texture of the FG Cu- 30 wt% Zn sample during uniaxial tensile deformation. It can be obviously seen that the extremely weak fiber texture of <110> // TD and the extremely strong <111> // TD fiber texture existed in the FG sample after tensile deformation. This confirms that the grain orientation in Cu- 30 wt% Zn alloy can be reoriented under uniaxial tension.

In literature, the pronounced deformation twinning was produced in grains oriented close to the <111> // tensile axis directions in other fcc materials with low SFEs, such as high manganese steel [77]. Interestingly, this phenomenon is also found in our
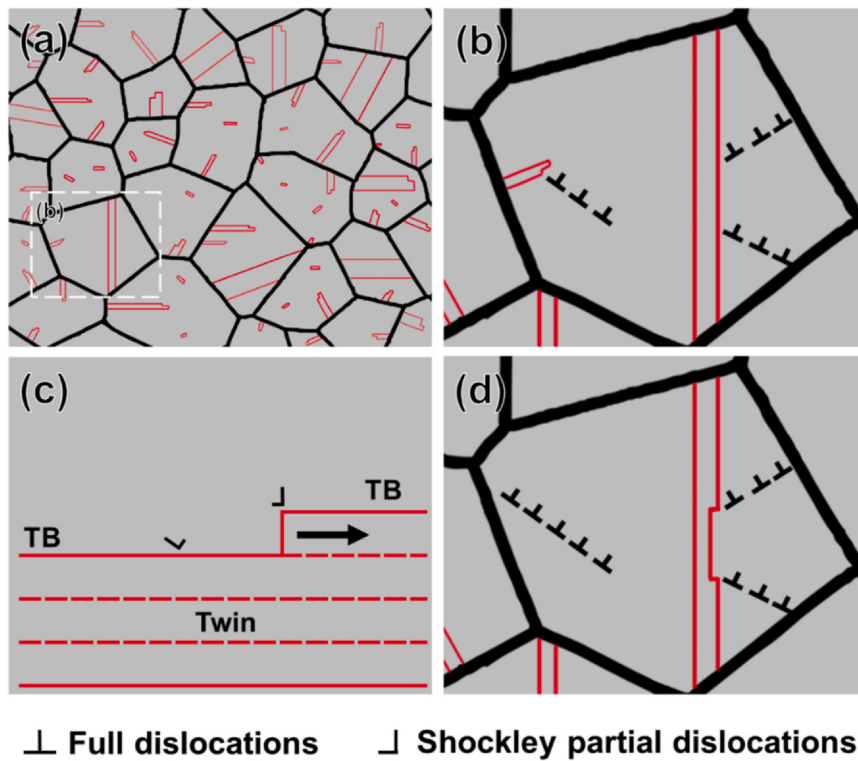
Fig. 14. (a) Schematic illustration of the initial microstructures of the FG sample before tensile test. The black and red lines depict HAGBs and pre-existing annealing TBs, respectively. (b-d) Schematic illustration of detwinning process through the interaction of the dislocation with the TB.
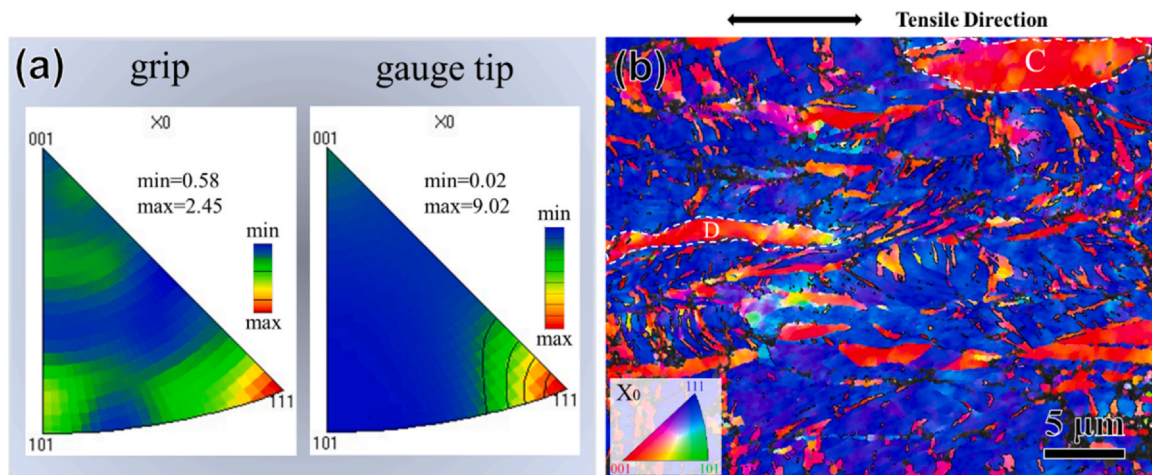
Fig. 15. (a) Inverse pole figures along TD of the FG Cu- 30 wt% Zn sample at grip (strain-free) and gauge part (strain of ~17%). (b) Crystal orientation map with twin boundaries (black lines) of the FG sample after 17% tension. IPF color of X_0 is applied, which is parallel to TD.

investigative Cu- 30 wt% Zn alloy. As shown in Fig. 15b, there are numerous parallel deformation twins in grains with orientation <111> // TD. On the contrary, grains with orientation <100> // TD are free of twins, for instance, grains C and D, indicating dislocation glide is more favorable relative to deformation twinning in these grains. Barbier et al. [51] reported that the Schmid factors for twinning are much less than dislocation glide in <100> // TD oriented grains. Similar results reported by Beladi et al. [54] that grains with <111> // TD orientation have a high Taylor factor and twinned in the early stage of tensile deformation, and grains with <100> // TD orientation have a low Taylor factor and did not twin up to fracture.

5. Conclusions

In this study, we prepared partially recrystallized, fine- and coarse-grained Cu- 30 wt% Zn alloys with the average grain sizes of 1.3 µm, 3.8 µm and 30.6 µm, respectively, by means of ECAP followed by annealing. Tensile testing indicated that both FG and CG samples possessed an excellent strain hardening capacity and drastic mechanical detwinning and twinning reflected by the phenomenon of stress serrations. The deformed samples at different strain levels were analyzed by EBSD and TEM to reveal the deformation mechanisms. The main conclusions are as following:

(1) The as-ECAPed Cu- 30 wt% Zn sample is consisted of numerous deformed structures containing high-density dislocations, LAGBs, deformation twins. After annealing, partial recrystallization occurred in the PR sample which is composed of deformed and recrystallized areas. The FG and CG samples contain fully recrystallized grains and high-density immature annealing twins (including corner, stepped and isolated twins).

(2) The FG sample exhibited superior combination of strength (YS of 250 MPa and UTS of 565 MPa) and ductility of 20%. The higher YS of the FG sample is attributed to high-density conventional HAGBs and TBs, and the outstanding strain hardening capacity is attributed to high fraction of HAGBs including pre-existing TBs, low dislocation densities, deformation-induced detwinning and pronounced deformation twinning.

(3) The total length of TBs in the FG sample first decreased and then increased under tension due to detwinning and twinning. EBSD statistics analysis revealed that ultrafine twin lamellae disappeared by the detwinning process, and micro twins annihilated via converting TBs into conventional HAGBs.

(4) Deformation twinning was a dominant deformation mechanism in both FG and CG samples under uniaxial tension. Grain orientation had great influence on the twinning process. All deformation twins were readily produced in grains with <111> orientation parallel to tensile direction.

CRediT authorship contribution statement

Lei Gu: Data curation, Visualization, Writing – original draft, revision, EBSD and TEM experiments and analyses. **Ningning Liang:** Supervision, Validation, Funding acquisition. **Yuyao Chen:** EBSD analysis. **Yonghao Zhao:** Investigation, Conceptualization, Supervision, Writing – review & editing, Funding acquisition.

Declaration of Competing Interest

The authors declare that they have no known competing financial interests or personal relationships that could have appeared to influence the work reported in this paper.

Acknowledgements

References

[1] Y.Z. Li, Z.Y. Liang, M.X. Huang, Strengthening contributions of dislocations and twins in warm-rolled TWIP steels, Int. J. Plast. 150 (2022) 103198.

[2] P. Chowdhury, D. Canadinc, H. Sehitoglu, On deformation behavior of Fe-Mn based structural alloys, Mater. Sci. Eng. R 122 (2017) 1–28.

[3] C. Wang, W. Cai, C. Sun, X. Li, L. Qian, J. Jiang, Strain rate effects on mechanical behavior and microstructure evolution with the sequential strains of TWIP steel, Mater. Sci. Eng. A 835 (2022) 142673.

[4] I. Gutierrez-Urrutia, S. Zaefferer, D. Raabe, The effect of grain size and grain orientation on deformation twinning in a Fe-22 wt% Mn-0.6 wt% C TWIP steel, Mater. Sci. Eng. A 527 (2010) 3552–3560.

[5] S. Cheng, H. Choo, Y.H. Zhao, X.L. Wang, Y.T. Zhu, Y.D. Wang, J. Almer, P.K. Liao, J.E. Jin, Y.K. Lee, High ductility in ultrafine-grained steel via phase transformation, J. Mater. Res. 23 (2008) 1578–1586.

[6] X.H. An, S.D. Wu, Z.G. Wang, Z.F. Zhang, Significance of stacking fault energy in bulk nanostructured materials: Insights from Cu and its binary alloys as model systems, Prog. Mater. Sci. 101 (2019) 1–45.

[7] Y.H. Zhao, Y.T. Zhu, X.Z. Liao, Z. Horita, T.G. Langdon, Tailoring stacking fault energy for high ductility and high strength in ultrafine grained Cu and its alloy, Appl. Phys. Lett. 89 (2006) 121906.

[8] Y.H. Zhao, X.Z. Liao, Z. Horita, T.G. Langdon, Y.T. Zhu, Determining the optimal stacking fault energy for achieving high ductility in ultrafine-grained Cu-Zn alloys, Mater. Sci. Eng. A 493 (2008) 123–129.

[9] P.C. Han, N.R. Tao, Effect of deformation mechanisms on the strength-ductility trade-off of Cu and CuAl alloy, Scr. Mater. 212 (2022) 114559.

[10] X.H. An, S.D. Wu, Z.F. Zhang, R.B. Figueiredo, N. Gao, T.G. Langdon, Enhanced strength-ductility synergy in nanostructured Cu and Cu-Al alloys processed by high-pressure torsion and subsequent annealing, Scr. Mater. 66 (2012) 227–230.

[11] X.Z. Gao, Y.P. Lu, J.Z. Liu, J. Wang, T.M. Wang, Y.H. Zhao, Extraordinary ductility and strain hardening of Cr$_{26}$Mn$_{20}$Fe$_{20}$Co$_{20}$Ni$_{14}$ TWIP high-entropy alloy by cooperative planar slipping and twinning, Materialia 8 (2019) 100485.

[12] Y. Kim, M. Kim, K. Lee, 1.45 GPa ultrastrong cryogenic strength with superior impact toughness in the in-situ nano oxide reinforced CrMnFeCoNi high-entropy alloy matrix nanocomposite manufactured by laser powder bed fusion, J. Mater. Sci. Technol. 97 (2022) 10–19.

[13] Y. Deng, C.C. Tasan, K.G. Pradeep, H. Springer, A. Kostka, D. Raabe, Design of a twinning-induced plasticity high entropy alloy, Acta Mater. 94 (2015) 124–133.

[14] Y. Zou, S. Li, S. Liu, J. Li, Y. Li, Improved mechanical and corrosion properties of CrMnFeCoNi high entropy alloy with cold rolling and post deformation annealing process, J. Alloy. Compd. 887 (2021) 161416.

[15] G. Laplanche, A. Kostka, O.M. Horst, G. Eggeler, E.P. George, Microstructure evolution and critical stress for twinning in the CrMnFeCoNi high-entropy alloy, Acta Mater. 118 (2016) 152–163.

[16] W. Jiang, X. Gao, Y. Cao, Y. Liu, Q. Mao, L. Gu, Y. Zhao, Charpy impact behavior and deformation mechanisms of Cr$_{26}$Mn$_{20}$Fe$_{20}$Co$_{20}$Ni$_{14}$ high-entropy alloy at ambient and cryogenic temperatures, Mater. Sci. Eng. A 837 (2022) 142735.

[17] W. Jiang, X. Gao, Y. Guo, X. Chen, Y. Zhao, Dynamic impact behavior and deformation mechanisms of Cr$_{26}$Mn$_{20}$Fe$_{20}$Co$_{20}$Ni$_{14}$ high-entropy alloy, Mater. Sci. Eng. A 824 (2021) 141858.

[18] A.J. Zaddach, C. Niu, C.C. Koch, D.L. Irving, Mechanical properties and stacking fault energies of NiFeCrCoMn high-entropy alloy, JOM 65 (2013) 1780–1789.

[19] C.Y. Yu, P.W. Kao, C.P. Chang, Transition of tensile deformation behaviors in ultrafine-grained aluminum, Acta Mater. 53 (2005) 4019–4028.

[20] B.B. Wang, G.M. Xie, L.H. Wu, P. Xue, D.R. Ni, B.L. Xiao, Y.D. Liu, Z.Y. Ma, Grain size effect on tensile deformation behaviors of pure aluminum, Mater. Sci. Eng. A 820 (2021) 141504.

[21] Y.H. Zhao, T. Topping, Y. Li, E.J. Lavernia, Strength and ductility of bi-modal Cu, Adv. Eng. Mater. 13 (2011) 865–871.

[22] A. Bolsonella, F. Naimi, O. Heintz, T. Tricone, H. Couque, F. Bernard, Influence of oxygen induced during high-energy ball milling process on the mechanical properties of sintered nickel by SPS, J. Alloy. Compd. 856 (2021) 157869.

[23] T.R. Lee, C.P. Chang, P.W. Kao, The tensile behavior and deformation microstructure of cryo-rolled and annealed pure nickel, Mater. Sci. Eng. A 408 (2005) 131–135.

[24] Y. Cao, S. Ni, X.Z. Liao, M. Song, Y.T. Zhu, Structural evolutions of metallic materials processed by severe plastic deformation, Mater. Sci. Eng. R 133 (2018) 1–59.

[25] Q. Mao, Y. Liu, Y. Zhao, A review on mechanical properties and microstructure of ultrafine grained metals and alloys processed by rotary swaging, J. Alloy. Compd. 896 (2022) 163122.

[26] I.A. Ovid'ko, R.Z. Valiev, Y.T. Zhu, Review on superior strength and enhanced ductility of metallic nanomaterials, Prog. Mater. Sci. 94 (2018) 462–540.

[27] L. Lu, X. Chen, X. Huang, K. Lu, Revealing the maximum strength in nanotwinned copper, Science 323 (2009) 607–610.

[28] Y.H. Zhao, J.F. Bingert, X.Z. Liao, B.Z. Cui, K. Han, A.V. Serhueeva, A.K. Muhkerjee, R.Z. Valiev, T.G. Langdon, Y.T. Zhu, Simultaneously elevating the ductility and strength of ultra-fine grained pure Cu, Adv. Mater. 18 (2006) 2949–2953.

[29] F.H. Duan, Y. Lin, J. Pan, L. Zhao, Q. Guo, D. Zhang, Y. Li, Ultrastrong nanotwinned pure nickel with extremely fine twin thickness, Sci. Adv. 7 (2021) eabg5113.

[30] X.Z. Gao, L.J. Dai, Y.H. Zhao, Twin boundary-dislocation interactions in nanocrystalline Cu-30% Zn alloys prepared by high pressure torsion, J. Mater. Res. Technol. 9 (2020) 11958–11967.

[31] X. Liu, M. Nakatani, H. Gao, B. Sharma, H. Pan, Z. Fu, X. Li, K. Ameyama, X. Zhu, Effect of stacking fault energy on deformation mechanisms in Cu and Cu-30% Zn alloy with gradient structure obtained by SMAT, J. Alloy. Compd. 865 (2021) 158863.

[32] M.J. Szczerba, M.S. Szczerba, Slip versus twinning in low and very low stacking-fault energy Cu-Al alloy single crystals, Acta Mater. 133 (2017) 109–119.

[33] S. Shi, L. Dai, Y. Zhao, Ternary relation among stacking fault energy, grain size and twin nucleation size in nanocrystalline and ultrafine grained CuAl alloys, J. Alloy. Compd. 896 (2021) 162953.

[34] Y.T. Zhu, X.Z. Liao, X.L. Wu, Deformation twinning in nanocrystalline materials, Prog. Mater. Sci. 57 (2012) 1–62.

[35] Y.T. Zhu, X.Z. Liao, X.L. Wu, J. Narayan, Grain size effect on deformation twinning and detwinning, J. Mater. Sci. 48 (2013) 4467–4475.

[36] Y.S. Li, L.J. Dai, Y. Cao, Y.H. Zhao, Y.T. Zhu, Grain size effect on deformation twin thickness in a nanocrystalline metal with low stacking-fault energy, J. Mater. Res. 34 (2019) 2398–2405.

[37] Y. Li, Y.H. Zhao, W. Liu, C. Xu, Z. Horita, X.Z. Liao, Y.T. Zhu, T.G. Langdon, E.J. Lavernia, Influence of grain size on the density of deformation twins in Cu-30%Zn alloy, Mater. Sci. Eng. A 527 (2010) 3942–3948.

[38] Y.H. Zhao, Z. Horita, T.G. Langdon, Y.T. Zhu, Evolution of defect structures during cold rolling of ultra-fine grained Cu and Cu-Zn alloys: influence of stacking fault energy, Mater. Sci. Eng. A 474 (2008) 342–347.

[39] Y.H. Zhao, Y.T. Zhu, X.Z. Liao, Z. Horita, T.G. Langdon, Influence of stacking fault energy on the minimum grain size achieved in severe plastic deformation, Mater. Sci. Eng. A 463 (2007) 22–26.

[40] Y.H. Zhao, X.Z. Liao, Y.T. Zhu, Z. Horita, T.G. Langdon, Influence of stacking fault energy on nanostructured formation by high pressure torsion, Mater. Sci. Eng. A 410–411 (2005) 188–193.

[41] T.J. Gao, D. Zhao, T.W. Zhang, T. Jin, S.G. Ma, Z.H. Wang, Strain-rate-sensitive mechanical response, twinning, and texture features of NiCoCrFe high-entropy alloy: Experiments, multi-level crystal plasticity and artificial neural networks modeling, J. Alloy. Compd. 845 (2020) 155911.

[42] J.W. Christian, S. Mahajan, Deformation twinning, Prog. Mater. Sci. 39 (1995) 1–157.

[43] M.J. Szczerba, S. Kopacz, M.S. Szczerba, Detwinning-twinning behavior during compression of face-centered cubic twin-matrix layered microstructure, Mater. Sci. Eng. A 795 (2020) 139960.

[44] M.J. Szczerba, S. Kopacz, M.S. Szczerba, Detwinning of face-centered cubic deformation twins via the correspondence matrix approach, Acta Mater. 102 (2016) 162–168.

[45] C. D'Hondt, V. Doquet, J.P. Couzinié, Direct monitoring of twinning/detwinning in a TWIP steel under reversed cyclic loading, Mater. Sci. Eng. A 814 (2021) 141250.

[46] Q. Xie, Y. Chen, P. Yang, Z. Zhao, Y. Wang, K. An, In-situ neutron diffraction investigation on twinning/detwinning activities during tension-compression load reversal in a twinning induced plasticity steel, Scr. Mater. 150 (2018) 168–172.

[47] S. Ni, Y.B. Wang, X.Z. Liao, H.Q. Li, R.B. Figueiredo, S.P. Ringer, T.G. Langdon, Y.T. Zhu, Effect of grain size on the competition between twinning and detwinning in nanocrystalline metals, Phys. Rev. B 84 (2011) 235401.

[48] S. Ni, Y.B. Wang, X.Z. Liao, S.N. Alhajeri, H.Q. Li, S.P. Ringer, T.G. Langdon, Y.T. Zhu, Grain size effect on deformation twinning and de-twinning in a nanocrystalline Ni-Fe alloy, Mater. Sci. Forum 667–669 (2011) 181–186.

[49] S. Cheng, Y. Zhao, Y. Wang, Y. Li, X. Wang, P.K. Liaw, E.J. Lavernia, Structure modulation driven by cyclic deformation in nanocrystalline NiFe alloy, Phys. Rev. Lett. 104 (2010) 255501.

[50] S. Cheng, Y. Zhao, Y. Guo, Y. Li, Q. Wei, X. Wang, Y. Ren, P.K. Liaw, H. Choo, E.J. Lavernia, High plasticity and substantial deformation in nanocrystalline alloys under dynamic loading, Adv. Mater. 21 (2009) 5001–5004.

[51] J. Wang, N. Li, O. Anderoglu, X. Zhang, A. Misra, J.Y. Huang, J.P. Hirth, Detwinning mechanisms for growth twins in face-centered cubic metals, Acta Mater. 58 (2010) 2262–2270.

[52] N. Li, J. Wang, A. Misra, X. Zhang, J.Y. Huang, J.P. Hirth, Twinning dislocation multiplication at a coherent twin boundary, Acta Mater. 59 (2011) 5989–5996.

[53] R.Z. Valiev, T.G. Langdon, Principles of equal-channel angular pressing as a processing tool for grain refinement, Prog. Mater. Sci. 51 (2006) 881–981.

[54] X.T. Fang, G.Z. He, C. Zheng, X.L. Ma, D. Kaoumi, Y.S. Li, Y.T. Zhu, Effect of heterostructure and hetero-deformation induced hardening on the strength and ductility of brass, Acta Mater. 186 (2020) 644–655.

[55] Y.H. Zhao, Y.Z. Guo, Q. Wei, A.M. Dangelewicz, C. Xu, Y.T. Zhu, T.G. Langdon, Y.Z. Zhou, E.J. Lavernia, Influence of specimen dimensions on the tensile behavior of ultrafine-grained Cu, Scr. Mater. 59 (2008) 627–630.

[56] Y.H. Zhao, Y.Z. Guo, Q. Wei, T.D. Topping, A.M. Dangelewicz, Y.T. Zhu, T.G. Langdon, E.J. Lavernia, Influence of specimen dimensions and strain measurement methods on tensile stress-strain curves, Mater. Sci. Eng. A 525 (2009) 68–77.

[57] T.H. Courney, Mechanical Behavior of Materials, seond ed., McGraw-Hill Companies, Inc, 2000.

[58] Y. Zhang, J.P. Liu, S.Y. Chen, X. Xie, P.K. Liaw, K.A. Dahmen, J.W. Qiao, Y.L. Wang, Serration and noise behaviors in materials, Prog. Mater. Sci. 90 (2017) 358–460.

[59] M. Knapek, P. Dobroň, K. Máthis, K. Illková, A. Mortensen, F. Chmelík, Occurrence of the Portevin Le-Châtelier effect in open-cell microcellular Al-2 wt% Mg, Scr. Mater. 132 (2017) 13–16.

[60] S. Lee, J. Kim, S.J. Lee, B.C. De, Cooman, Effect of Cu addition on the mechanical behavior of austenitic twinning-induced plasticity steel, Scr. Mater. 65 (2011) 1073–1076.

[61] H. Gao, Y. Huang, W.D. Nix, J.W. Hutchinson, Mechanism-based strain gradient plasticity—I. Theory, J. Mech. Phys. Solids 47 (1999) 1239–1263.

[62] L.P. Kubin, A. Mortensen, Geometrically necessary dislocations and strain-gradient plasticity: a few critical issues, Scr. Mater. 48 (2003) 119–125.

[63] Y.F. Liu, Y. Cao, Q.Z. Mao, H. Zhou, Y.H. Zhao, W. Jiang, Y. Liu, J.T. Wang, Z.S. You, Y.T. Zhu, Critical microstructures and defects in heterostructured materials and their effects on mechanical properties, Acta Mater. 189 (2020) 129–144.

[64] B. Gao, Q.Q. Lai, Y. Cao, R. Hu, L.R. Xiao, Z.Y. Pan, N.N. Liang, Y.S. Li, G. Sha, M.P. Liu, H. Zhou, X.L. Wu, Y.T. Zhu, Ultrastrong low-carbon nanosteel produced by heterostructure and interstitial mediated warm rolling, Sci. Adv. 6 (2020) eaba8169.

[65] X.L. Wu, M.X. Yang, F.P. Yuan, G.L. Wu, Y.J. Wei, X.X. Huang, Y.T. Zhu, Heterogeneous lamella structure unites ultrafine-grain strength with coarse-grain ductility, Proc. Natl. Acad. Sci. USA 112 (47) (2015) 14501–14505.

[66] Y.T. Zhu, K. Ameyama, P.M. Anderson, I.J. Beyerlein, H.J. Gao, H.S. Kim, E. Lavernia, S. Mathaudhu, H. Mughrabi, R.O. Ritchie, N. Tsuji, X.Y. Zhang, X.L. Wu, Heterostructured materials: superior properties from hetero-zone interaction, Mater. Res. Lett. 9 (1) (2021) 1–31.

[67] Y.T. Zhu, X.L. Wu, Perspective on hetero-deformation induced (HDI) hardening and back stress, Mater. Res. Lett. 7 (10) (2019) 393–398.

[68] X. Luo, Z.Q. Feng, T.B. Yu, J.Q. Luo, T.L. Huang, G.L. Wu, N. Hansen, X.X. Huang, Transitions in mechanical behavior and in deformation mechanisms enhance the strength and ductility of Mg-3Gd, Acta Mater. 183 (2020) 398–407.

[69] H. Somekawa, D.A. Basha, A. Singh, Role of grain boundaries on ductility in Mg-Y alloys, Materialia 8 (2019) 100466.

[70] F. Wagner, A. Ouarem, T. Richeton, L.S. Toth, Improving mechanical properties of cp titanium by heat treatment optimization, Adv. Eng. Mater. 20 (2018) 1700237.

[71] Y.T. Zhu, X.L. Wu, X.Z. Liao, J. Narayan, L.J. Kecskés, S.N. Mathaudhu, Dislocation-twin interactions in nanocrystalline fcc metals, Acta Mater. 59 (2011) 812–821.

[72] G. Tsukamoto, T. Kunieda, S. Yamasaki, M. Mitsuhara, H. Nakashima, Effects of temperature and grain size on active twinning systems in commercially pure titanium, J. Alloy. Compd. 884 (2021) 161154.

[73] D.D. Li, L.H. Qian, C.Z. Wei, S. Liu, F.C. Zhang, J.Y. Meng, The role of Mn on twinning behavior and tensile properties of coarse- and fine-grained Fe-Mn-C twinning-induced plasticity steels, Mater. Sci. Eng. A 789 (2020) 139586.

[74] D. Barbier, N. Gey, S. Allain, N. Bozzolo, M. Humbert, Analysis of the tensile behavior of a TWIP steel based on the texture and microstructure evolutions, Mater. Sci. Eng. A 500 (2009) 196–206.

[75] I. Gutierrez-Urrutia, D. Raabe, Dislocation and twin substructure evolution during strain hardening of an Fe-22wt%Mn-0.6wt%C TWIP steel observed by electron channeling contrast imaging, Acta Mater. 59 (2011) 6449–6462.

[76] V. Shterner, A. Molotnikov, I. Timokhina, Y. Estrin, H. Beladi, A constitutive model of the deformation behaviour of twinning induced plasticity (TWIP) steel at different temperatures, Mater. Sci. Eng. A 613 (2014) 224–231.

[77] H. Beladi, I.B. Timokhina, Y. Estrin, J. Kim, B.C. De Cooman, S.K. Kim, Orientation dependence of twinning and strain hardening behaviour of a high manganese twinning induced plasticity steel with polycrystalline structure, Acta Mater. 59 (2011) 7787–7799.